ACS OMEGA

http://pubs.acs.org/journal/acsodf

Article

Wet Catalytic Oxidation of a FeMnCe-Activated Semi-Coke Catalyst for Treating Piperazine Wastewater

Kaiwen Ren, Shuo Liu, Zhiyu Dong, and Junfeng Wang*

Cite This: *ACS Omega* 2023, 8, 8683−8694

Read Online

ACCESS | Metrics & More | Article Recommendations

ABSTRACT: A FeMnCe-activated semi-coke catalyst (FeMnCe/ASC) was prepared by the co-precipitation method using semi-coke as the raw material. The structure and morphology were characterized by X-ray diffraction, Brunauer−Emmett−Teller, scanning electron microscopy, and transmission electron microscopy analyses. The catalytic activity and stability of the FeMnCe/ASC catalyst were investigated with piperazine as the target degradation pollutant and ammonia nitrogen and chemical oxygen demand (COD) as the evaluation indexes. The results showed that the average pore size of FeMnCe/ASC mesopores was 6.68 nm, and the active components were uniformly dispersed on the carrier surface. Under the optimum conditions of piperazine solution including a mass concentration of 100 mg/L, a catalyst mass concentration of 4.0 g/L, a reaction temperature of 240 °C, an oxygen partial pressure of 1.2 MPa, a stirring speed of 500 rpm, and a reaction time of 120 min, the degradation rates of both ammonia nitrogen and COD reached 100%. After the catalyst was recycled five times, the degradation rates of ammonia nitrogen and COD still reached more than 90%. The elemental valence changes before and after the reaction were analyzed by X-ray photoelectron spectroscopy, and the intermediate products generated from piperazine degradation were analyzed by gas chromatography−mass spectroscopy to evaluate the mechanism of piperazine degradation and speculate about the degradation pathway of piperazine.

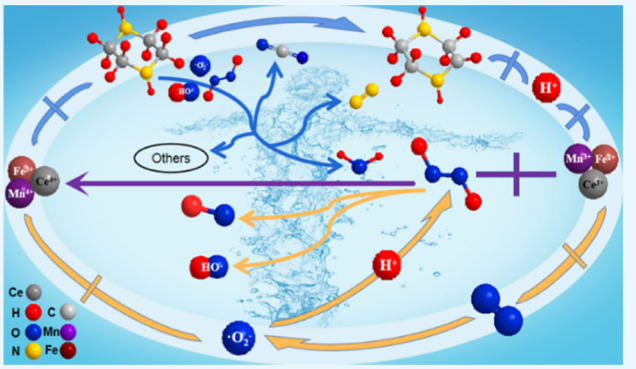

Piperazine wastewater is a difficult-to-degrade industrial organic wastewater produced by pharmaceutical and other industrial processes. Piperazine wastewater contains a large amount of organic components containing NH_3−N moieties and is also accompanied by high chemical oxygen demand (COD) values in the water column.[1−3] Moreover, it is extremely biotoxic and difficult to degrade and has been prioritized for monitoring and control in countries around the world.[4] The main treatment methods for piperazine wastewater include physical, chemical, and biological methods.[5,6] Physical methods such as adsorption and precipitation can only separate piperazine from water and are prone to secondary contamination; in contrast, biological methods are prone to inactivation by poisoning, leading to their limited application.[7] In recent years, advanced oxidation processes (AOPs) have been favored by many researchers due to their advantages including a fast reaction rate and final degradation products such as N_2, CO_2, and H_2O.[8−10]

Catalytic wet air oxidation (CWAO) has attracted significant research attention as an AOP with the advantages including a fast oxidation efficiency, wide application range, and no solid waste generation.[11] The method usually involves the oxidative degradation of organic pollutants in wastewater by passing oxygen under high-temperature (225−320 °C) and high-pressure (5−20 MPa) conditions. The addition of catalysts can effectively alleviate the harsh operating conditions such as temperature and pressure in the CWAO process. The commonly used catalysts are based on metals such as Ru, Cu, Fe, Co, Mn, Ni, and Ce.[12] Among them, Fe-based catalysts are one of the current research hotspots because of their advantages such as low cost and environmental friendliness. Therefore, many researchers have used Fe-based catalysts to treat phenol wastewater, dye wastewater, etc. Nonetheless, the degradation of piperazine wastewater by CWAO technology with this catalyst has rarely been reported to date. The commonly selected carriers for Fe-based catalysts include alumina-, clay-, and carbon-based materials. Among them, carbon-based materials have been widely noticed because of their low cost and good catalytic performance.[13−15] Moreover, among all the carbon-based materials, semi-coke (SC) is the

Received: December 19, 2022
Accepted: February 13, 2023
Published: February 22, 2023

most inexpensive, with a high carbon content, good pore structure, strong reactivity with O_2, and capable of undergoing easy modification and is a good catalyst carrier. However, it was found that activated SC needs to be activated to have a high utilization value.

To this end, in this study, FeMnCe-activated SC (FeMnCe/ASC) was prepared by the co-precipitation method using SC as the raw material, and its performance in wet catalytic oxidative degradation of ammonia nitrogen and COD in piperazine wastewater was evaluated. Furthermore, the process parameters of piperazine degradation were investigated. Finally, the mechanism of piperazine degradation was analyzed by X-ray photoelectron spectroscopy (XPS) experiments combined with gas chromatography−mass spectroscopy (GC−MS), and the possible degradation pathways of piperazine were speculated.

1. EXPERIMENTAL SECTION

1.1. Materials and Equipment. Ferric nitrate nonahydrate [$Fe(NO_3)_3{\cdot}9H_2O$], manganese nitrate hexahydrate [$Mn(NO_3)_2{\cdot}6H_2O$], cerium nitrate hexahydrate [$Ce(NO_3)_2{\cdot}6H_2O$], sodium carbonate (Na_2CO_3), piperazine, hydrofluoric acid (HF), potassium hydroxide (KOH), nitric acid (HNO_3), and all analytical grade reagents were used in the experiments and obtained from Sinopharm Chemical Reagent Co., Ltd. Experimental water was secondary deionized water, homemade in the laboratory. SC was obtained from ChuangYu Energy Technology Co., Shenmu City, Shaanxi Province, China.

The structure and morphology of the samples were characterized using various techniques including X-ray diffraction (XRD) (D/max 2500X, RIKEN, Japan); N_2 adsorption and desorption analysis [BSD-PS1, Bayside Instrument Technology (Beijing) Co., Ltd.]; transmission electron microscopy (TEM, JEM-2010, Japan Electronics Corporation); scanning electron microscopy (SEM, JSM-7800F, Japan Electronics Corporation); XPS (AXIS ULTRA DLD, Tsushima, Japan); and GC−MS (Agilent model 5977B, Agilent Technologies, Inc.).

1.2. Catalyst Preparation.

(1) Carrier preparation: Half of the coke from the Shaanxi region was used as the carrier, and the other half was crushed to a 200 mesh and set aside. SC powder (5 g) was taken, and remove it with HF (20 mL, 10%). It was then filtered and washed until neutral. Subsequently, it was dried at 80 °C for 2 h, impregnated with aqueous KOH solution (45 mL, 5 mol/L) for 2 h, filtered, washed until neutral, and finally dried at 80 °C for 2 h. After drying, the sample was placed in a quartz boat, and N_2 was passed through the tube furnace. The sample was then activated at 800 °C for 2 h with a heating rate of 5 °C/min and then heated, which resulted in the formation of the modified active SC (ASC).

(2) Catalyst preparation: The metal ion nitrate was weighed proportionally, an appropriate amount of deionized water was added, and the contents were stirred thoroughly. Next, an excess of anhydrous Na_2CO_3 was weighed and dissolved in deionized water. A certain amount of deionized water was heated to 75 °C and stirred; when the water temperature became stable at 75 °C, the metal nitrate and Na_2CO_3 were added dropwise into the beaker using a peristaltic pump, and the flow of Na_2CO_3 was adjusted to maintain the pH in the range of 7−8. At the end of dropwise addition, the pH was maintained in the range of 7−8. After the dropwise addition, precipitate aging was carried out at room temperature, and it was washed until no NO_3^- was left behind and dried at 80 °C, and ground ASC was added. Next, HNO_3 solution (1 mol/L) was continuously added during the grinding process, and after sufficient grinding, the sample was dried at 80 °C and taken out. Finally, it was roasted at 450 °C for 4 h in a muffle furnace, and FeMnCe/ASC was obtained after roasting.

1.3. Catalyst Characterization. The XRD test was conducted with a Cu target at a voltage of 40 kV, a current of 100 mA, a fast scan speed of 4°/min, and a scan range of 5−85°. The Brunauer−Emmett−Teller (BET) test was conducted at a liquid nitrogen temperature of −196.15 °C. The SEM test was carried out at a scan voltage of 220 V, a temperature setting of (20 ± 5) °C, and a relative humidity of <80%. The TEM analysis was performed at an accelerating voltage of 200 kV, using a copper mesh film. XPS was carried out with an X-ray source using a Mg Kα source, and vacuum of the analysis chamber was 5×10^{-5} Pa.

The experimental setup for the catalytic wet oxidation reaction, shown in Figure 1, was used to evaluate the performance of the catalyst. The degradation experimental procedure is as follows: The piperazine wastewater (300 mL, 100 mg/L) and catalyst (1.20 g) were accurately measured and carefully added to an autoclave. Next, the reaction kettle was fixed and purged three times with nitrogen gas to evacuate the air inside the kettle. After electric heating to the set temperature, a certain amount of oxygen was introduced into the kettle. The oxygen-filled moment was recorded as the reaction start time, and samples were taken every 5−10 min. The intermediate products of the reaction were analyzed using a GC−MS analyzer, and the NH_3−N mass concentration in the wastewater was determined by the colorimetric method with the GB-7479-87 nano-reagent. The NH_3−N mass concentration was obtained by measuring the absorbance at 405 nm. The COD mass concentration in the wastewater was determined by the potassium dichromate method (GB11914-89) in the range of 30−700 mg/L. The COD removal rate was calculated as follows

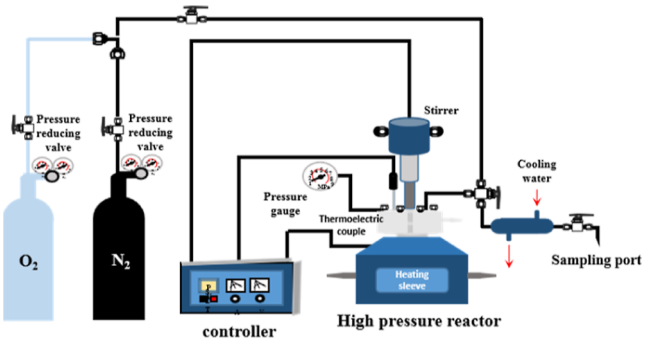

Figure 1. Schematic showing CWAO equipment.

$$r/\% = \frac{\rho_0 - \rho}{\rho_0} \times 100 \quad (1)$$

where r is the COD removal rate, %; ρ_0 is the initial COD mass concentration, mg/L; and ρ is the post-reaction COD mass concentration, mg/L.

https://doi.org/10.1021/acsomega.2c08074
ACS Omega 2023, 8, 8683−8694

2. RESULTS AND DISCUSSION

2.1. Characterization of the Catalyst. The XRD spectra of SC, ASC, Fe/ASC, FeMn/ASC, and FeMnCe/ASC are shown in Figure 2. The characteristic peaks at 2θ = 26.6 and

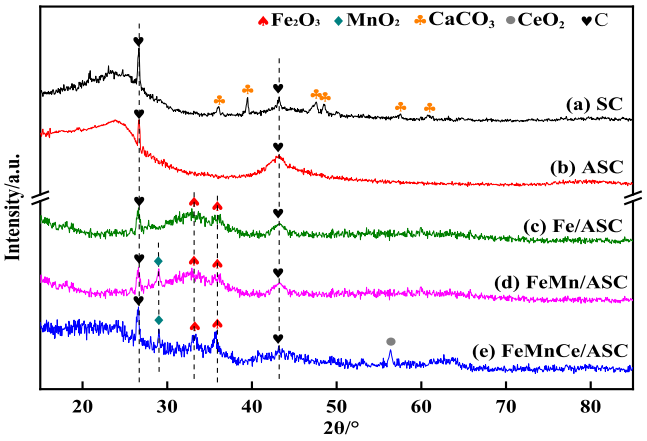

Figure 2. XRD patterns of catalysts: (a) SC; (b) ASC; (c) Fe/ASC; (d) FeMn/ASC; and (e) FeMnCe/ASC.

43.2° for hemijoules (SC) correspond to the (002) and (101) crystallographic planes of graphitic carbon, respectively (JCPDS nos. 41-1487).[16] Moreover, the peaks at 2θ = 35.9, 39.9, 47.3, 48.4, 57.4, and 60.6° correspond to the (110), (113), (018), (116), (122), and (214) crystallographic planes of calcite (JCPDS nos. 86-2339), respectively. The characteristic peaks of ASC at 2θ = 26.6 and 43.2° also correspond to the (002) and (101) crystallographic planes of the graphite lamellar structure, respectively, but the characteristic peaks of calcite disappear. It indicates that most of the mineral components of the SC were processed after the deliming and thermal activation treatment to form an ASC. The characteristic peaks of Fe/ASC at 2θ = 33.1 and 35.6°, in addition to the retention of the characteristic peaks of ASC, show that the main component of iron oxide is Fe_2O_3, which corresponds to the (110) and (113) crystal faces of Fe_2O_3, respectively (JCPDS nos. 87-1166).[17] The characteristic peak of FeMn/ASC at 2θ = 28.6° is attributed to the (110) crystal plane of MnO_2 (JCPDS nos. 71-0071), and part of the diffraction peak of the manganese oxide is masked by the iron oxide peak, indicating that the manganese oxide grains are very fine and well dispersed. The FeMnCe/ASC material retains the basic characteristic peak of FeMn/ASC in addition to the characteristic peak at 2θ = 56.5°, which is attributed to the (311) crystal plane of CeO_2 (JCPDS nos. 78-0694). The characteristic peaks of ASC, Fe_2O_3, MnO_2, and CeO_2 were observed for the FeMnCe/ASC material, indicating the successful preparation of the material.

Figure 3 shows the adsorption−desorption curves and pore size distributions of SC, ASC, Fe/ASC, FeMn/ASC, and FeMnCe/ASC. Figure 3 demonstrates that all the above-mentioned samples conform to the type IV adsorption isotherm, indicating that the materials consist of a mesoporous structure. The hysteresis loop of SC is H3-type, and this type of hysteresis loop is typical of mineral materials. The hysteresis loops of ASC, Fe/ASC, FeNi/ASC, and FeNiCe/ASC all belong to the H4 type, and H4 type hysteresis loops are commonly found in carbon materials containing mesoporous structure characteristics. This result clearly indicates that most of the minerals are removed from the modified materials to form carbon materials containing a mesoporous structure.

Table 1 presents the BET specific surface area and pore structure parameters of SC, ASC, Fe/ASC, FeMn/ASC, and FeMnCe/ASC. Table 1 summarizes that the specific surface area, pore volume, and average pore size of SC are 30.68 m^2/g, 0.16 cm^3/g, and 4.48 nm, respectively. The specific surface area, pore volume, and average pore size of SC increased to 319.26 m^2/g, 0.56 cm^3/g, and 7.83 nm, respectively, after modification, which may be attributed to the removal of impurities present on the material surface during the modification process by acid−base and heat treatment, resulting in the increase in these values. The specific surface areas of Fe/ASC, FeMn/ASC, and FeMnCe/ASC decreased to 297.11, 276.32, and 263.53 m^2/g, respectively, and the pore volumes decreased by 0.54, 0.51, and 0.49 cm^3/g, while the average pore sizes decreased to 7.36, 6.85, and 6.68 nm, respectively. This result can be attributed to the change of pore structure blockage by the increase of active components; however, the catalytic performance was improved as indicated by the comparative analysis. It indicates that the decrease in specific surface area did not affect the catalyst activity, and in contrast, it shows that the catalysts doped with different elements have higher activity.

Figure 4 shows the SEM image of SC, ASC, and FeMnCe/ASC. The results showed that there were significant differences in the microscopic surface morphology of the SC before and after the activation treatment. At the same magnification, the SC showed a relatively flat surface, while a large number of pores of different sizes were formed on the surface of the activated SC, with recognizable grooves between the layers, and the pore sizes inside the SC were enlarged accordingly. As shown in Figure 4c,d, the FeMnCe/ASC catalyst shows a porous structure similar to that of an "anthill" with dense pores and well-developed pore channels, and the active components are spherically attached to the catalyst surface and pore channels, blocking some of the pore channels and thus reducing the specific surface area of the loaded catalyst. Data analysis confirmed this.

Figure 5 shows TEM images at different magnifications. Figure 5a illustrates that the Fe_2O_3 particle size is between 90 and 100 nm, and many small particles are observed to be aggregated on the catalyst surface. They are uniformly dispersed on the carrier surface and are analyzed to be MnO_2 and CeO_2 in the catalyst, which are present in a highly dispersed form.[18] Figure 5b shows the TEM image of the lattice streaks of the catalyst. The red box shows the lattice streaks of Fe_2O_3, which exhibits a lattice streak of d = 0.204 nm as derived from the lattice spacing. The lattice stripe with a d of 0.204 nm corresponds to 110 crystalline planes, as indicated by XRD analysis, which is consistent with the XRD results. Figure 5c shows the lattice stripes of MnO_2 and CeO_2. The lattice stripes of MnO_2 are d = 0.308 nm, which corresponds to the 110 crystal plane of MnO_2, while the lattice stripes of CeO_2 are d = 0.163 nm, which corresponds to the 311 crystal plane of CeO_2, which is also consistent with the XRD results.

2.2. Process Optimization. The effects of temperatures of 180, 200, 220, 240, and 260 °C on the degradation of ammonia nitrogen and COD in piperazine wastewater by CWAO were investigated at an initial mass concentration of 150 mg/L of piperazine, a mass concentration of 4.0 g/L of the catalyst, a reaction time of 180 min, and a stirring speed of 500 $rpm \cdot min^{-1}$, and the results are shown in Figure 6.

https://doi.org/10.1021/acsomega.2c08074
ACS Omega 2023, 8, 8683−8694

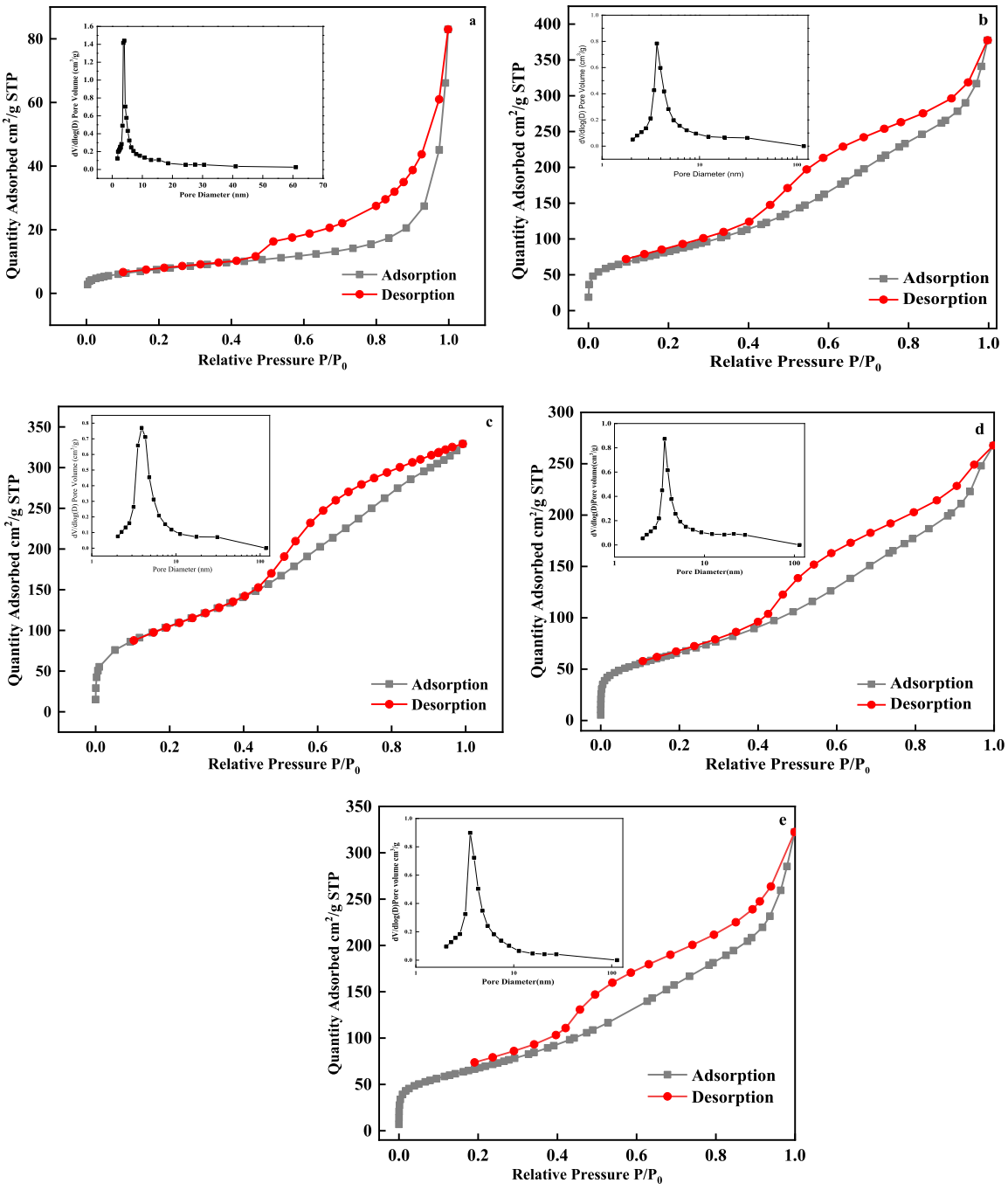

Figure 3. N_2 adsorption−desorption isotherm curve and pore size distribution (a) SC; (b) ASC; (c) Fe/ASC; (d) FeMn/ASC; and (e) FeMnCe/ASC.

Table 1. List of Specific Surface Area, Pore Volume, and Pore Size

catalyst	S_{BET} (m^2/g)	pore volume (cm^3/g)	average pore size/(nm)
SC	30.68	0.16	4.48
ASC	319.26	0.56	7.83
Fe/ASC	297.11	0.54	7.36
FeMn/ASC	276.32	0.51	6.85
FeMnCe/ASC	263.53	0.49	6.68

Figure 6a illustrates that the removal rates of ammonia nitrogen from piperazine wastewater were 36.21, 63.21, 91.22, 100, and 100% at 180, 200, 220, 240, and 260 °C, respectively. At 180 and 200 °C, the removal rates of ammonia nitrogen were 0 for 80 and 40 min before the reaction, respectively, which is possibly due to the fact that piperazine wastewater is organic ammonia nitrogen wastewater, which should be first converted into free NH_3 and NH_4^+. Therefore, under the temperature conditions of 180 and 200 °C, the ammonia nitrogen content still exhibited an increasing trend in the early stage of the reaction, and the degradation had not yet started. Figure 6b demonstrates that the COD removal rates were 78.21, 90.23, 100, 100, and 100% at 180, 200, 220, 240, and 260 °C, respectively. When the reaction temperature was below 240 °C, the temperature was positively correlated with the removal rates of ammonia nitrogen and COD; however,

https://doi.org/10.1021/acsomega.2c08074
ACS Omega 2023, 8, 8683−8694

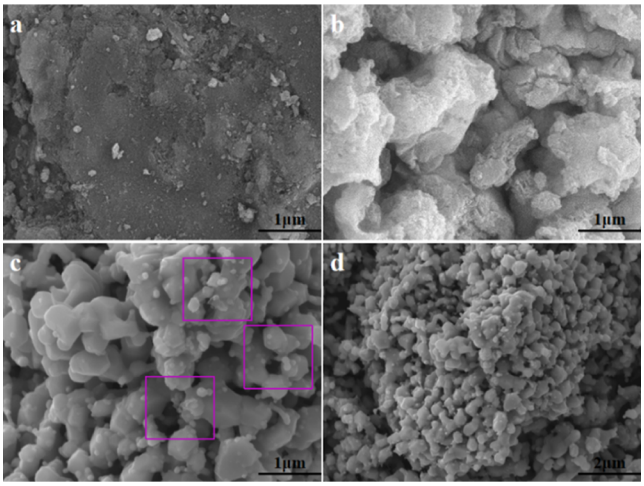

Figure 4. (a) SC, (b) ASC, and (c,d) FeMnCe/ASC catalyst SEM.

when it exceeded 240 °C, the COD removal rate was not significantly enhanced. Therefore, the reaction temperature of 240 °C was selected as the optimal value for further experiments.

After determining the reaction temperature of CWAO to degrade ammonia nitrogen and COD in piperazine wastewater, catalytic oxidation experiments were conducted at oxygen partial pressures of 0.6, 0.8, 1.0, 1.2, and 1.4 MPa to investigate the effect of oxygen pressure on ammonia nitrogen and COD in piperazine wastewater, and the results are shown in Figure 7.

Figure 7a exhibits that when the partial pressure of oxygen was 0.6 and 0.8 MPa, the removal rate of ammonia nitrogen was 75.26 and 93.25%, respectively, after 180 min of the reaction. When the partial pressure of oxygen was increased to 1.0 MPa, the ammonia nitrogen was completely removed after 140 min of the reaction. However, with the continuous increase in the partial pressure of oxygen to 1.2 and 1.4 MPa, the ammonia nitrogen was removed within 120 min. Figure 7b demonstrates that when the partial pressure of oxygen was 0.6 and 0.8 MPa, the COD removal rate was 86.21 and 100%, respectively, for the reaction time of 180 min. With the increase in the partial pressure of oxygen to 1.0 MPa, the COD removal rate reached 100% for the reaction time of 140 min. In contrast, when the partial pressure of oxygen was continued to increase to 1.2 and 1.4 MPa, for the reaction time of 120 min, the COD was completely removed. The change trend of COD in piperazine wastewater was basically the same as that of ammonia nitrogen. When the partial pressure of oxygen was increased from 1.2 to 1.4 MPa, the removal rate of COD and ammonia nitrogen in piperazine wastewater almost did not change, probably because the oxygen concentration in the solution did not reach saturation at P_{O_2} for a longer period. However, after reaching a certain value, the main oxygen concentration in the liquid phase was stabilized by the stabilization of the catalyst surface. The oxygen diffusion rate no longer controlled the reaction process; as a result, the oxygen partial pressure of 1.2 MPa was selected as the optimal value for the experiment.

After determining the optimized partial pressure of oxygen, piperazine solutions with concentrations of 50, 100, 150, 200, and 250 mg/L were prepared to investigate the changes of ammonia nitrogen and COD in different piperazine concentrations, and the results are shown in Figure 8.

Figure 8a illustrates that when the initial concentration of piperazine was 50 mg/L, the removal rate could reach 97.38% after 180 min of the reaction. When it was increased to 100 mg/L, the removal rate of ammonia nitrogen was 100% after 120 min of the reaction. However, with the increase in the initial concentration of piperazine to 150 mg/L, the removal rate of ammonia nitrogen was 100% after 180 min of the reaction. With the further increase in the initial concentration of piperazine to 200 mg/L, the removal rate of ammonia nitrogen was 78.23%, and then, the conversion rate of ammonia nitrogen began to decrease. With the continuous increase in the concentration of piperazine to 250 mg/L, the removal rate of ammonia nitrogen decreased to 35.22%, and the decrease rate increased significantly. Analysis of the COD removal shown in Figure 8b indicates that when the piperazine concentration was increased from 50 to 100 mg/L, the COD removal rate increased from 95.21 to 100%; however, with the further increase in the piperazine concentration from 100 to 250 mg/L, the COD removal rate decreased from 100 to 53.99%, which corresponds to larger decrease. This is attributed to the fact that as the concentration increases, more intermediate products are generated, and these products consume the reaction active material, thus leading to a decrease in the removal rate. Furthermore, under the same catalyst dosage, the relative dosage of the catalyst actually decreased with the increase in the initial concentration of piperazine, which also contributed to the decrease of ammonia and COD removal rates. Therefore, the maximum concentration of degraded piperazine was 100 mg/L corresponding to 300 mL volume at a certain reaction temperature, reaction pressure, and catalyst dosage.

After determining the optimum piperazine concentration of 100 mg/L, catalysts with mass concentrations of 1.0, 2.0, 3.0, 4.0, and 5.0 g/L were added to investigate the effect of the catalyst mass concentration on the removal of ammonia nitrogen and COD from piperazine.

Figure 9a shows that the ammonia nitrogen removal rates in the piperazine wastewater were 23.98, 88.21, 100, 100, 100, 100, and 100% after 180 min of the reaction for catalyst mass concentrations of 1.0, 2.0, 3.0, 4.0, and 5.0 g/L. Among these

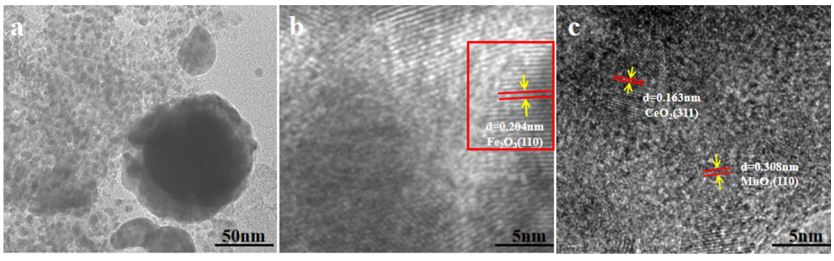

Figure 5. (a–c) FeMnCe/ASC catalyst TEM at different magnifications.

https://doi.org/10.1021/acsomega.2c08074
ACS Omega 2023, 8, 8683−8694

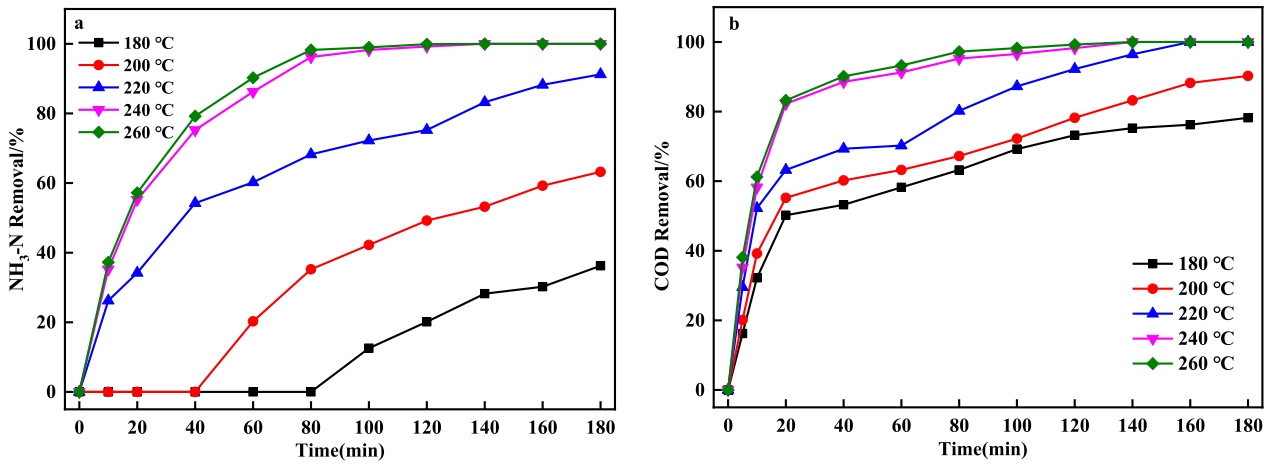

Figure 6. (a) Effects of reaction temperature on NH_3−N removal. (b) Effects of reaction temperature on COD removal.

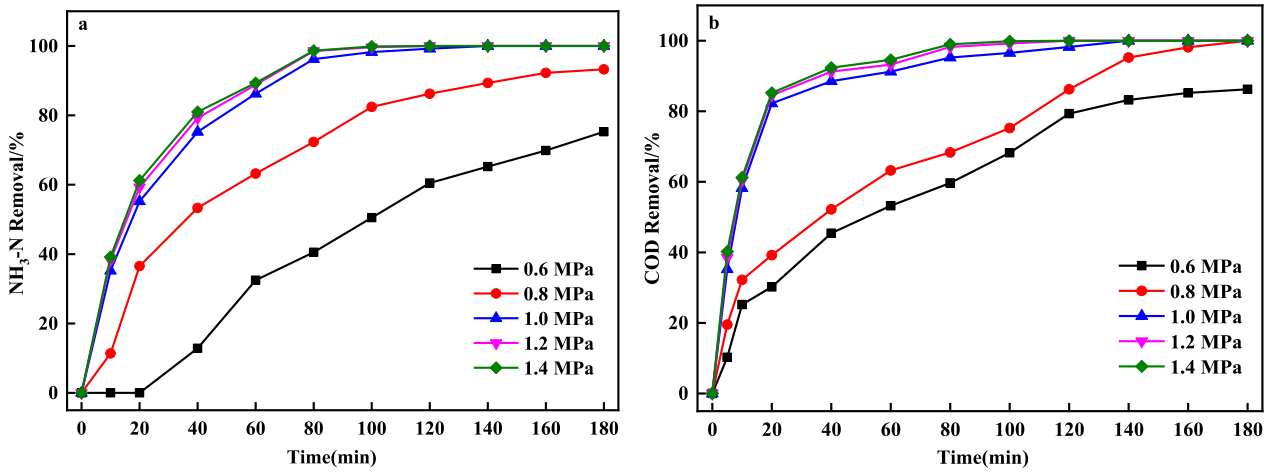

Figure 7. (a) Effects of reaction pressure on NH3−N removal. (b) Effects of reaction pressure on COD removal.

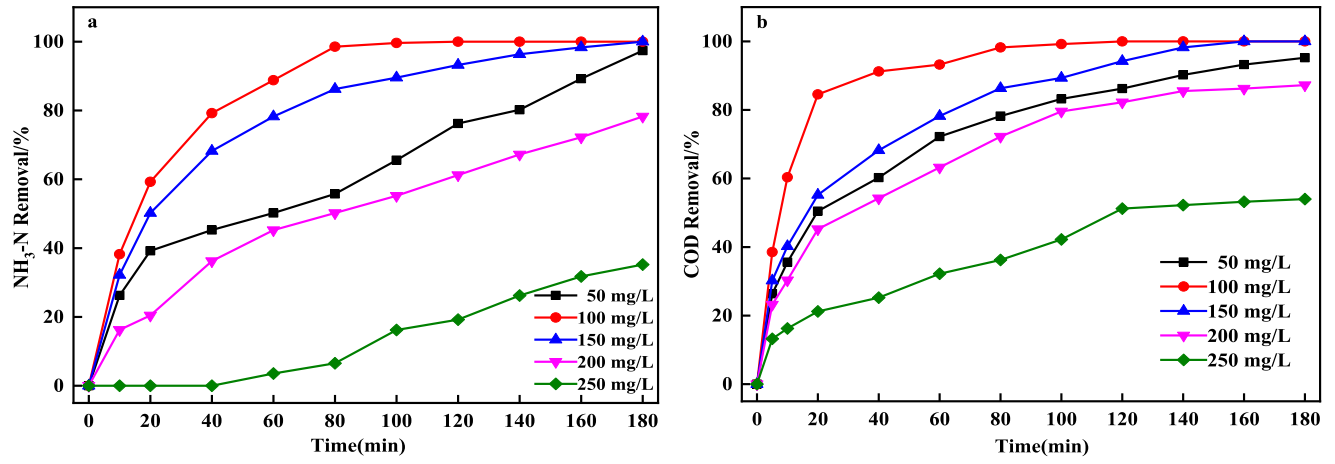

Figure 8. (a) Effects of the initial concentration on NH_3−N removal. (b) Effects of the initial concentration on COD removal.

conditions, when the catalyst dosage was 4.0 and 5.0 g/L and the reaction proceeded for 120 min, the ammonia nitrogen removal rates were all 100%, and the reaction tended to be at equilibrium at this time. Figure 9b exhibits that the COD removal rates were 47.26, 96.21, 100, 100, 100, 100, and 100% after 180 min of the reaction for catalyst mass concentrations of 1.0, 2.0, 3.0, 4.0, and 5.0 g/L, and the trend similar to that for the ammonia nitrogen removal rate was observed. The COD removal rate was 100% at 120 min. In combination with the degradation of ammonia nitrogen and COD, the removal rate of ammonia nitrogen and COD increased with the increase of catalyst dosage. When the catalyst dosage was above 4 g/L, the improvement in the ammonia nitrogen and COD removal rate was not obvious, indicating that the ammonia nitrogen and COD removal rate had reached

https://doi.org/10.1021/acsomega.2c08074
ACS Omega 2023, 8, 8683−8694

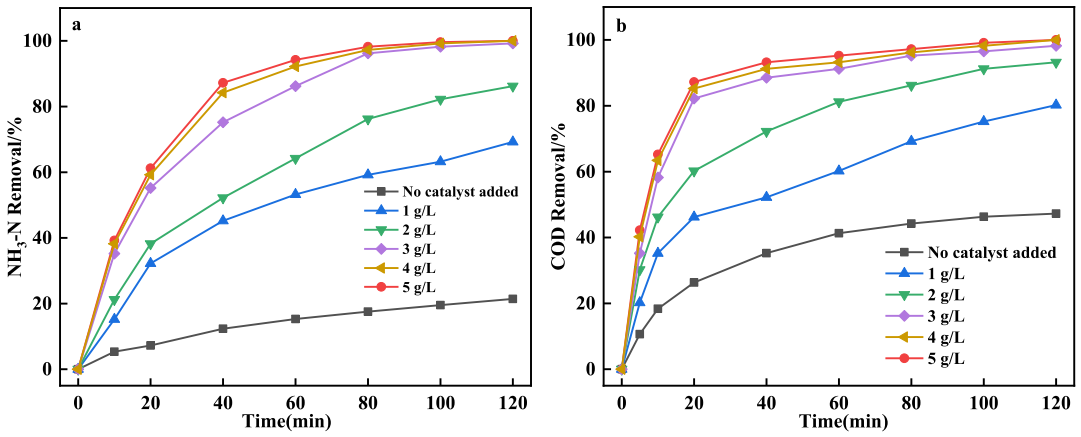

Figure 9. (a) Effects of catalyst dosage on NH_3−N removal. (b) Effects of catalyst dosage on COD removal.

saturation at this time, and thus, 4 g/L was selected as the best catalyst dosage for the CWAO reaction.

2.3. Mechanism of Piperazine Degradation. Figure 10 shows the full spectrum of FeMnCe/ASC and the high-resolution spectra of C 1s, O 1s, Fe 2p, Mn 2p, and Ce 3d. The figure clearly exhibits the existence of electronic peaks of Fe, Mn, Ce, O, and C elements, which are consistent with the actual composition of FeMnCe/ASC and are in good agreement with the XRD results. Figure 10b shows the XPS patterns of the 1s orbitals of O. The peaks with binding energies at 529.59, 531.39, and 533.34 eV are attributed to lattice oxygen (O^{2-}), atomic adsorbed oxygen (O^-), and molecular adsorbed oxygen O_2^- on the catalyst surface, respectively. The figure clearly illustrates that lattice oxygen is the main form present in the system. The percentage of peak area of O^{2-} increased from 45.39 to 65.90% after the reaction. The percentage of peak area of atomic adsorbed oxygen O^- decreased from 32.29 to 25.13%, while the percentage of peak area of molecular adsorbed oxygen O_2^- decreased from 15.31 to 8.98%. According to the literature,[19] O^{2-} is very unstable and easily migrates, and oxygen atoms get easily adsorbed in oxygen vacancies on the surface of metal oxides or get coordinated with metal atoms to undergo chemisorption, which facilitates catalytic reactions. Figure 10c shows the XPS pattern of the 1s orbital of C. The peaks located at binding energies of 284.40, 285.50, 287.7, and 290.20 eV are attributed to C−C, C═C, C═O, and O−C═O, respectively. The percentages of peak area of C−C and C═C groups after the reaction decrease from 49.77 and 27.27% to 31.64 and 23.27%, respectively. However, the peak area percentage of C═O and O−C═O groups increased from 11.81 and 11.15% to 28.70 and 16.39%, respectively. It indicates the possibility of the generation of free radicals during the reaction, breaking of the C−C and C═C bonds, and the reaction of the free radicals with the reactive oxygen species in the system to form C═O and O−C═O groups. Figure 10d demonstrates that the peak at 709.8 eV is the characteristic peak of the Fe $2p_{3/2}$ spin orbital of Fe^{2+}. The peaks at 711.50 and 724.00 eV are attributed to the characteristic peaks of the Fe $2p_{3/2}$ and Fe $2p_{1/2}$ spin orbitals, respectively, and the peak at 718.20 eV corresponds to the satellite peak of the Fe $2p_{3/2}$ orbital. The peak area percentage of Fe^{3+} accounts for 82.90% after the reaction, which is 21.43% higher than that before the reaction, and the Fe^{3+} content increases, indicating that the catalyst still shows high activity after the reaction.[20] The XPS spectra and fitted curves of the 2p orbitals of Mn are shown in Figure 10e. The spectral peaks at 642.3 and 652.6 eV correspond to the Mn $2p_{3/2}$ and Mn $2p_{1/2}$ orbitals of Mn^{4+} in the FeMnCe/ASC catalyst, respectively. The spectral peak at 640.7 eV corresponds to the Mn $2p_{3/2}$ orbitals of Mn^{3+} in the FeMnCe/ASC catalyst. It indicates that Mn exists in the form of Mn^{4+} and Mn^{3+}. The percentage of peak area of Mn^{4+} increased from 42.24 to 66.8% before the reaction, while the percentage of peak area of Mn^{3+} decreased from 57.76 to 33.2% before the reaction. Based on the analysis of related literature studies,[21] it was speculated that it was possibly due to the conversion of Mn^{4+} to Mn^{3+} after the degradation of piperazine by the active species Mn on the catalyst, while the active oxygen species on the catalyst contributed to reconversion to Mn^{4+}. Moreover, O_2 in the system gets adsorbed on the oxygen vacancies on the surface of each catalyst to replenish the oxygen active species in the catalyst system, and the reaction on the catalyst forms a cycle. Moreover, the increase in the proportion of Mn^{4+} is beneficial to the catalytic activity of the catalyst. Figure 10f shows the 3d orbital XPS spectra and fitted curves of Ce. The peaks at 881.48, 885.36, 888.53, and 897.82 eV are the characteristic peaks of Ce $3d_{5/2}$ spin orbitals. The peaks located at 900.83, 903.82, and 907.17 eV are the characteristic peaks of Ce $3d_{3/2}$ spin orbitals, and the peak at 916.27 eV is the satellite peak of Ce $3d_{3/2}$. Among them, Ce^{3+} corresponds to the peaks at 885.36 and 903.82 eV, and Ce^{4+} corresponds to peaks other than those of Ce^{3+}. The results of peak area calculation indicate that the percentage of Ce^{4+} is 74.36% and that of Ce^{3+} is 25.37% before the reaction, while the percentage of Ce^{4+} is 78.64% and that of Ce^{3+} is 21.36% after the reaction, and the content of Ce^{4+} increases. This result is possibly attributed to the fact that Ce^{3+} is partially oxidized to Ce^{4+} during the reaction, and the results of a literature study[22] showed that Ce^{4+} is the effective active component. Notably, Ce^{4+} provides more oxygen vacancies for the reaction, produces more chemisorbed oxygen, and thus promotes the rapid reaction of CWAO. It was thus presumed that the catalyst could still show high activity after the reaction.

The main mechanism of CWAO for the removal of organic matter is a free radical reaction mechanism. Based on XPS analysis of elemental valence changes before and after the reaction, herein, we speculated on the possible reaction mechanism, as shown Figure 11, which is represented by eqs

https://doi.org/10.1021/acsomega.2c08074
ACS Omega 2023, 8, 8683−8694

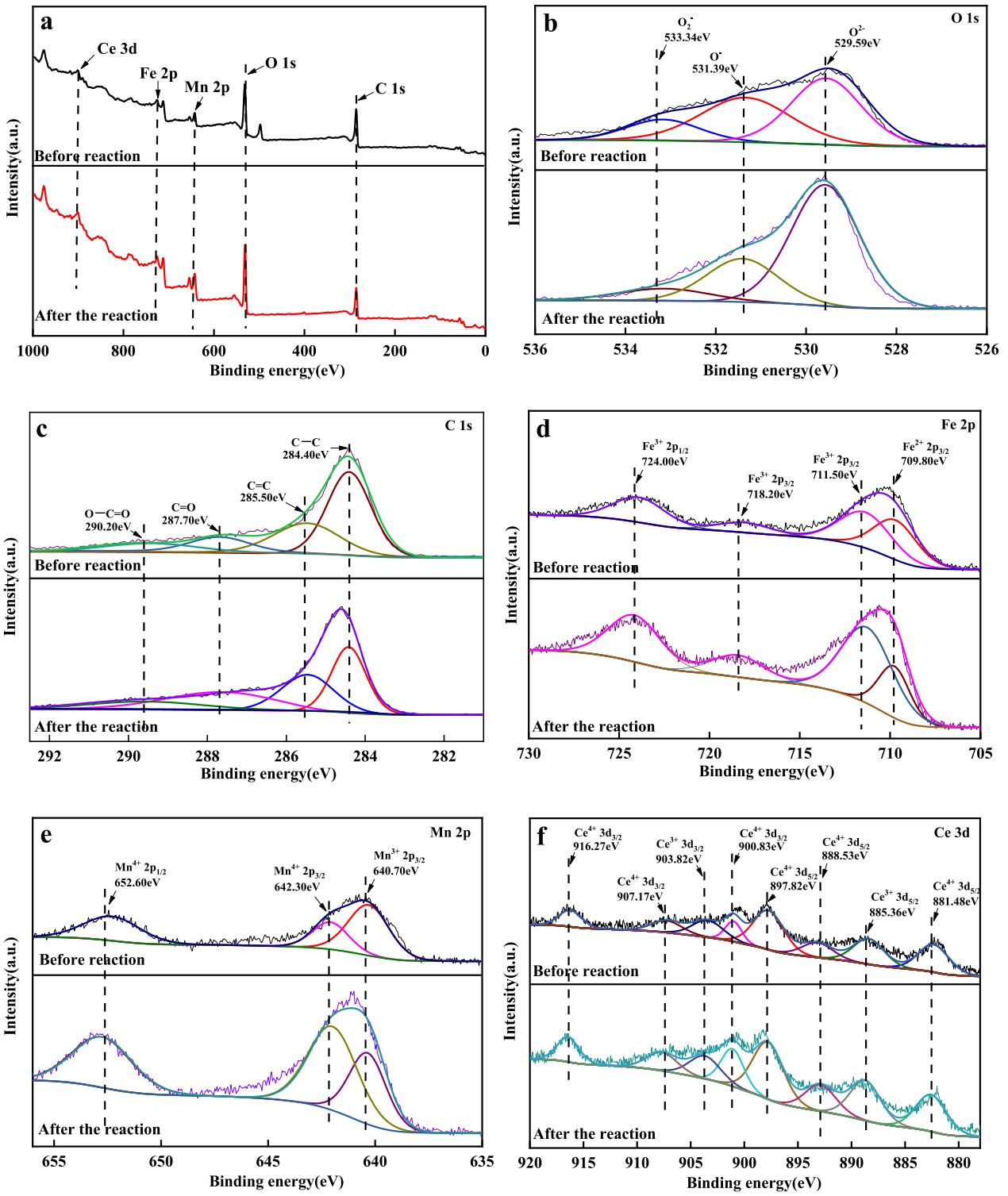

Figure 10. XPS spectra were scanned before and after the reaction of different catalysts: (a) whole scanning spectra; (b) O 1s; (c) C 1s Ru 3d; (d) Fe 2p; (e) Mn 2p; and (f) Ce 3d.

2−6 when using FeMnCe/ASC catalysts, where RH is organic matter and M denotes metals Fe, Mn, and Ce.

$$RH + Mn^{+} \rightarrow {}^{\bullet}R + H^{+} + M^{(n-1)+} \quad (2)$$

$$M^{(n-1)+} + O_2 \rightarrow {}^{\bullet}O_2^{-} + Mn^{+} \quad (3)$$

$$2H^{+} + 2{}^{\bullet}O_2^{-} \rightarrow O_2 + H_2O_2 \quad (4)$$

$$M^{(n-1)+} + H_2O_2 \rightarrow {}^{\bullet}OH + OH^{-} + Mn^{+} \quad (5)$$

$$RH + {}^{\bullet}OH \rightarrow CO_2 + H_2O + N_2 \quad (6)$$

The valence changes of Fe, Mn, and Ce give the FeMnCe/ASC catalysts excellent electron transfer properties and catalytic oxidation activity. The low-valent metal $M^{(n-1)+}$ captures O_2 to form ${}^{\bullet}O_2^{-}$ oxide species.[23] In addition, ${}^{\bullet}O_2^{-}$

https://doi.org/10.1021/acsomega.2c08074
ACS Omega 2023, 8, 8683−8694

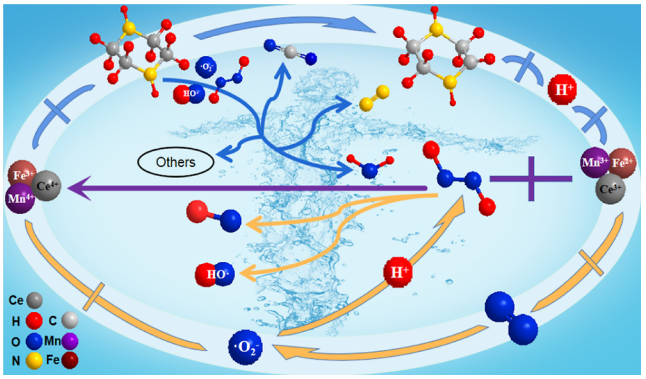

Figure 11. Mechanism of FeMnCe/ASC degradation of piperazine.

binds to H^+ in solution, thus providing some stronger oxidizing species such as H_2O_2. H_2O_2 binds to $M^{(n-1)+}$ to produce $^{\bullet}OH$, OH^-, and M^{n+}, and the presence of strong oxide species in CWAO reactions has become a consensus among experts. In the catalytic oxidation reaction of organic matter, Fu et al.[24] and Wang et al.[25] also confirmed the presence of strong oxidizing species $^{\bullet}O_2^-$, H_2O_2, and $^{\bullet}OH$ to oxidize organic matter into smaller molecules such as CO_2, H_2O, and other small organic molecules. In addition, according to the literature,[26] the N element of organic matter is decomposed to N_2 by strongly oxidizing substances at high temperature and pressure.

2.4. Quenching Experiment. Tertiary butanol (TBA) is the most widely used $^{\bullet}OH$ inhibitor. Different concentrations of TBA were added to the piperazine solution to verify that the main active substance for the degradation of ammonia nitrogen and COD in piperazine was $^{\bullet}OH$ by the burst reaction process, and the results are shown in Figure 12.

From Figure 12, it can be seen that the effect of CWAO in degrading ammonia nitrogen and COD in piperazine decreased significantly when the mass concentration of TBA increased from 0 to 80 mg/L. When the mass concentration of TBA was 80 mg/L and the reaction was carried out up to 120 min, the removal rates of ammonia nitrogen and COD in piperazine decreased from 100 to 6.83% and 9.36%, respectively, compared with no TBA addition. The possible reason is that the reaction of TBA with $^{\bullet}OH$ produces highly selective or inert intermediate substances, which make TBA strongly inhibit $^{\bullet}OH$ and terminate the $^{\bullet}OH$ oxidation reaction. The greater the concentration of TBA in the solution, the stronger the inhibitory effect. Therefore, it can be inferred from the strong inhibitory effect of TBA on $^{\bullet}OH$ that $^{\bullet}OH$ mainly plays an oxidizing role in the degradation of ammonia nitrogen and COD in piperazine by CWAO.

2.5. Piperazine Degradation Pathway. In conjunction with the piperazine degradation mechanism, in order to deduce the degradation pathway of piperazine by FeMnCe/ASC within the catalytic wet oxidation system, GC−MS was used to analyze the intermediate products of the piperazine degradation process. The parent ion mass spectra of the extracted individual substances are shown in Figure 13. The catalytic reaction was carried out at the initial piperazine concentration of 150 mg/L, a reaction temperature of 240 °C, P_{O_2} = 1.2 MPa, and a FeMnCe/ASC dose amount of 4.0 g/L. The aliquot of reaction solution at 10 min was taken for the GC−MS test. The results indicate that 2-hydroxypiperazine, [(2-aminoethyl)amino]acetaldehyde, ethylenediamine, glycine, ethanoic acid, oxalic acid, formaldehyde, and formic acid intermediates were produced during the degradation of piperazine. It indicates that the degradation of piperazine might have undergone multiple degradation steps.

Based on the literature studies,[27,28] the degradation history of piperazine was postulated, as shown in Figure 14. The mechanistic analysis indicates that the active substance $^{\bullet}OH$ was generated during the catalytic wet oxidation of piperazine by FeMnCe/ASC. Furthermore, in the presence of $^{\bullet}OH$, 2-hydroxy-piperazine (1) was subsequently formed, which underwent ring-opening oxidation to form [(2-aminoethyl)-amino]acetaldehyde (2). However, [(2-aminoethyl)amino]-acetaldehyde (2) was found to be unstable[29] and formed formaldehyde (8), oxalic acid (3), and ethylenediamine (4) by N−C bond breaking. The ethylenediamine continued to degrade to produce glycine (5) and ethanoic acid (6), which further produced oxalic acid (3) and formaldehyde, further forming formic acid (9). The final conversion products included CO_2, H_2O, and N_2.

2.6. Reusability of Catalysts. To examine the catalyst stability, six reusability experiments were conducted on the same batch of catalysts.[30] The loss rate of catalysts after each recovery was calculated to be between 1 and 2%, which is small, and thus, the catalysts are suitable for reuse after recovery. Their performance in catalytic wet oxidation of ammonia nitrogen and COD in piperazine was examined, and

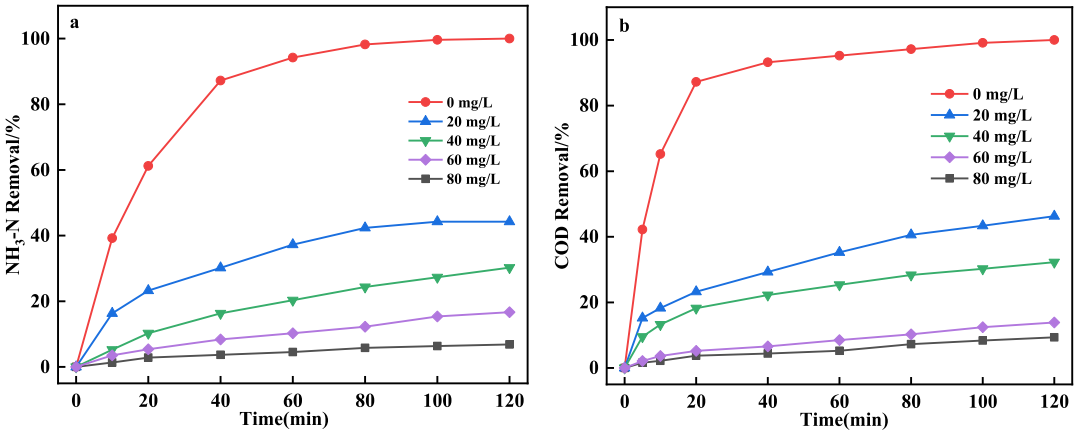

Figure 12. (a) Effects of TBA dosage on NH_3−N removal. (b) Effects of TBA dosage on COD removal.

https://doi.org/10.1021/acsomega.2c08074
ACS Omega 2023, 8, 8683−8694

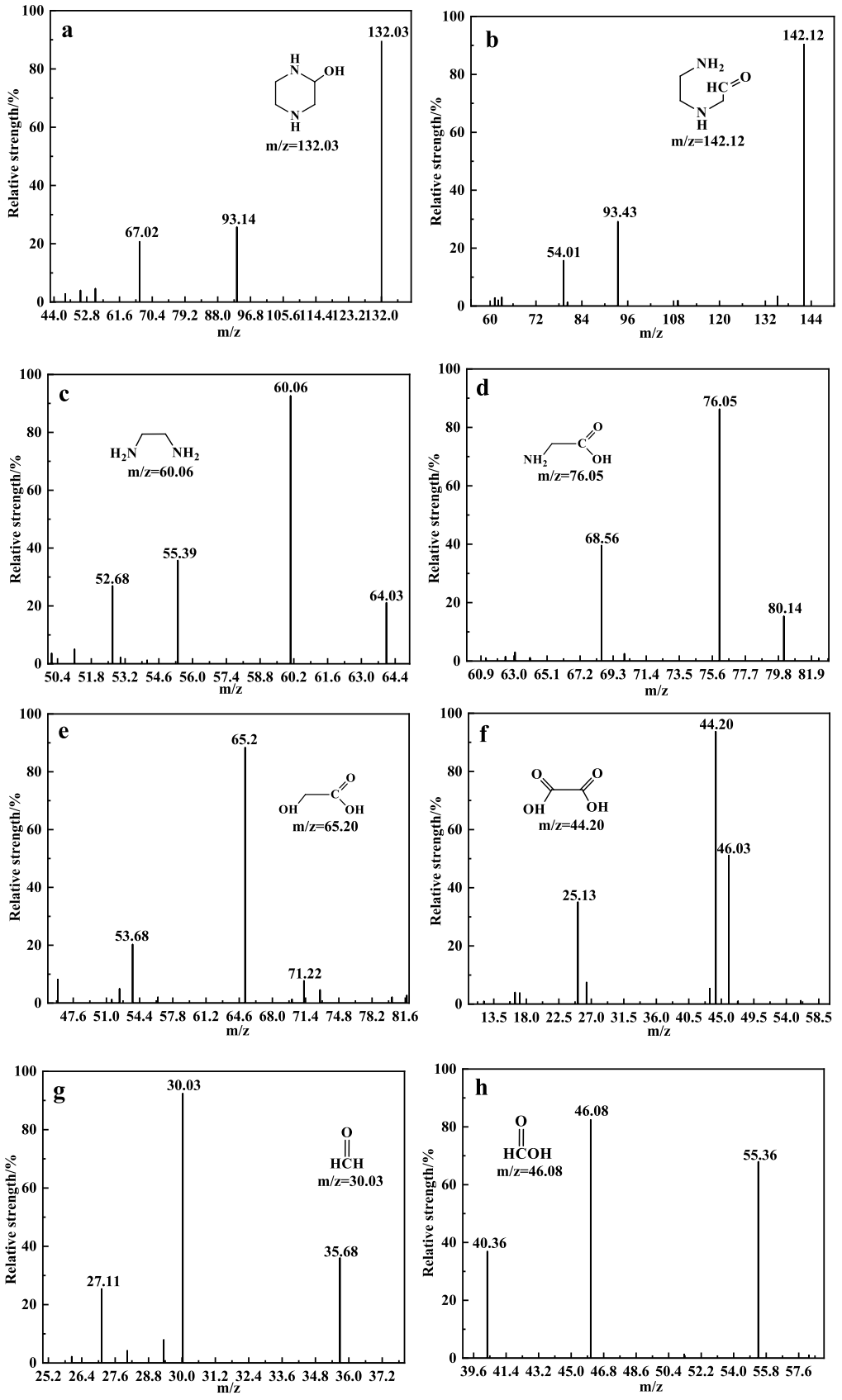

Figure 13. Mass spectrum of the main intermediate products: (a−h) 2-hydroxypiperazine, [(2-aminoethyl)amino]acetaldehyde, ethylenediamine, glycine, ethanoic acid, oxalic acid, formaldehyde, and formic acid.

the corresponding results are shown in Figure 15. The figure illustrates that the ammonia nitrogen and COD removal rates were 98.6 and 99.6%, respectively, when the catalyst was reused for the first time. Under the same conditions, the

https://doi.org/10.1021/acsomega.2c08074
ACS Omega 2023, 8, 8683−8694

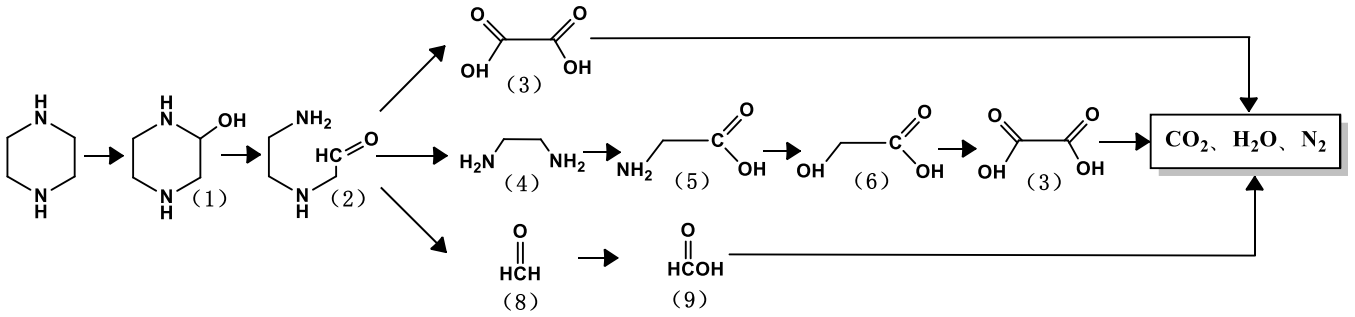

Figure 14. Degradation of piperazine by FeMnCe/ASC.

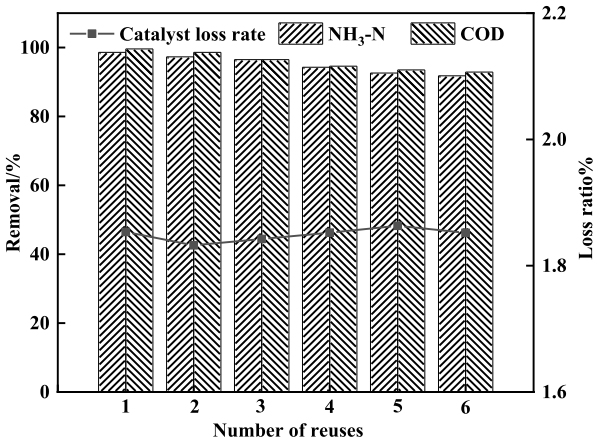

Figure 15. Recycling of FeMnCe/ASC.

ammonia nitrogen and COD removal rates could still reach more than 90% when the experiment was continued for five repetitions. It proved that the FeMnCe/ASC material is a stable non-homogeneous catalyst that can be effectively reused in catalytic wet oxidation for the degradation of ammonia nitrogen and COD in piperazine wastewater.

3. CONCLUSIONS

In this study, the wet catalytic oxidation of the FeMnCe-activated SC catalyst was carried out for treating piperazine wastewater. Based on the results, the following conclusions can be drawn: (1) The catalyst characterization analysis showed that FeMnCe/ASC exhibited a specific surface area of 263.53 m^2/g, a pore volume of 0.49 cm^3/g, and an average pore size of 6.68 nm. Moreover, the catalyst still showed a high activity after the reaction. (2) The optimum process conditions for the wet catalytic oxidation degradation of piperazine are as follows: a reaction temperature of 240 °C, a piperazine concentration of 100 mg/L, a catalyst dosage of 4.0 g/L, an oxygen partial pressure of 1.2 MPa, a reaction time of 120 min, and a rotational speed of 500 rpm; under these conditions, the removal rate of ammonia nitrogen and COD from piperazine reached 100%. The removal rate of ammonia nitrogen and COD in piperazine wastewater could still reach more than 90% after the catalyst was used five times. (3) The degradation history of piperazine was speculated by the mechanistic analysis and by testing the piperazine degradation intermediates by GC−MS. The active substance •OH was generated during the catalytic wet oxidation of piperazine by FeMnCe/ASC, and in the presence of •OH, 2-hydroxy-piperazine was subsequently formed. Furthermore, 2-hydroxy-piperazine underwent ring-opening oxidation and formed [(2-aminoethyl)amino]acetaldehyde, which was unstable and formed formaldehyde, oxalic acid, and ethylenediamine possibly by breaking of the N−C bond. The degradation of ethylenediamine led to the formation of glycine and ethanoic acid, which further formed oxalic acid and formaldehyde, further producing formic acid. The final conversion products were found to be CO_2, H_2O, and N_2.

AUTHOR INFORMATION

Corresponding Author

Junfeng Wang − *College of Mining and Technology, Taiyuan University of Technology, Taiyuan 030024, China;* orcid.org/0000-0003-2317-4014; Email: wangjunfeng@tyut.edu.cn

Authors

Kaiwen Ren − *College of Mining and Technology, Taiyuan University of Technology, Taiyuan 030024, China*

Shuo Liu − *School of Safety and Emergency Management Engineering, Taiyuan University of Technology, Taiyuan 030024, China*

Zhiyu Dong − *College of Mining and Technology, Taiyuan University of Technology, Taiyuan 030024, China*

Complete contact information is available at: https://pubs.acs.org/10.1021/acsomega.2c08074

Author Contributions

This manuscript was written through contributions of all authors. All authors have given approval to the final version of the manuscript.

Notes

The authors declare no competing financial interest.

ACKNOWLEDGMENTS

The authors gratefully acknowledge financial support from the National Natural Science Foundation of China (52074188).

REFERENCES

(1) Lai, Q.; Cai, T.; Tsang, S. C. E.; Chen, X.; Ye, R.; Xu, Z.; Argyle, M. D.; Ding, D.; Chen, Y.; Wang, J.; Russell, A. G.; Wu, Y.; Liu, J.; Fan, M. Chemical Looping Based Ammonia Production Promising Pathway for Production of the Noncarbon Fuel. *Sci. Bull.* **2022**, *67*, 2124−2138.

(2) Liu, S.; Qian, T.; Wang, M.; Ji, H.; Shen, X.; Wang, C.; Yan, C. Proton-Filtering Covalent Organic Frameworks with Superior Nitrogen Penetration Flux Promote Ambient Ammonia Synthesis. *Nat. Catal.* **2021**, *4*, 322−331.

(3) Wu, Z. Y.; Karamad, M.; Yong, X.; Huang, Q.; Cullen, D. A.; Zhu, P.; Xia, C.; Xiao, Q.; Shakouri, M.; Chen, F. Y.; Kim, J. Y.; Xia, Y.; Heck, K.; Hu, Y.; Wong, M. S.; Li, Q.; Gates, I.; Siahrostami, S.;

https://doi.org/10.1021/acsomega.2c08074
ACS Omega 2023, 8, 8683−8694

Wang, H. Electrochemical Ammonia Synthesis via Nitrate Reduction on Fe Single Atom Catalyst. *Nat. Commun.* **2021**, *12*, 2870.
(4) El-Khalafy, S. H.; Hassanein, M. T.; Abd-Elal, M. F.; Atia, A. A. Oxidation of Azo Dye Orange II with Hydrogen Peroxide Catalyzed by 5,10,15,20-Tetrakis[4-(Diethylmethylammonio)Phenyl]-Porphyrinato-Cobalt(II)Tetraiodide in Aqueous Solution. *J. Saudi Chem. Soc.* **2020**, *24*, 520−526.
(5) Villegas, L.; Mashhadi, N.; Chen, M.; Mukherjee, D.; Taylor, K. E.; Biswas, N. A short review of techniques for phenol removal from wastewater. *Curr. Pollut. Rep.* **2016**, *2*, 157−167.
(6) Dai, Y.; Liu, M.; Li, J.; Yang, S.; Sun, Y.; Sun, Q.; Wang, W.; Lu, L.; Zhang, K.; Xu, J.; Zheng, W.; Hu, Z.; Yang, Y.; Gao, Y.; Liu, Z. A review on pollution situation and treatment methods of tetracycline in groundwater. *Sep. Sci. Technol.* **2020**, *55*, 1005−1021.
(7) Patel, T.; Mayani, V. J.; Mayani, S. V. Development of a Sustainable Tungsten and Iron Bimetal Immobilized SBA-15 Composite for Enhanced Wet Catalytic. *ACS Omega* **2022**, *8*, 346−356.
(8) Feng, J. Y.; Ning, P.; Li, K.; Sun, X.; Wang, C.; Jia, L. J.; Fan, M. H. One-Step Synthesis of Ammonia Directly from Wet Air/N_2 by Plasma Combined with a γ-Al_2O_3 Catalyst. *ACS Sustainable Chem. Eng.* **2023**, *11*, 804−814.
(9) Hassani, A.; Eghbali, P.; Mahdipour, F.; Wacławek, S.; Lin, K. Y. A.; Ghanbari, F. Insights into the synergistic role of photocatalytic activation of peroxymonosulfate by UVA-LED irradiation over $CoFe_2O_4$-rGO nanocomposite towards effective Bisphenol A degradation: Performance, mineralization, and activation mechanism. *Chem. Eng. J.* **2023**, *453*, 139556.
(10) Karim, A. V.; Hassani, A.; Eghbali, P.; Nidheesh, P. V. Nanostructured modified layered double hydroxides (LDHs)-based catalysts: A review on synthesis, characterization, and applications in water remediation by advanced oxidation processes. *Curr. Opin. Solid State Mater. Sci.* **2022**, *26*, 100965.
(11) Zhou, L.; Cao, H.; Descorme, C.; Xie, Y. Phenolic compounds removal by wet air oxidation-based processes. *Front. Environ. Sci. Eng.* **2018**, *12*, 1.
(12) Tews, I. J.; Garcia-Perez, M. Advanced Oxidative Techniques for the Treatment of Aqueous Liquid Effluents from Biomass Thermochemical Conversion Processes: A Review. *Energy Fuels* **2022**, *36*, 60.
(13) Madihi-Bidgoli, S.; Asadnezhad, S.; Yaghoot-Nezhad, A.; Hassani, A. Azurobine degradation using Fe_2O_3@multi-walled carbon nanotube activated peroxymonosulfate (PMS) under UVA-LED irradiation: performance, mechanism and environmental application. *J. Environ. Chem. Eng.* **2021**, *9*, 106660.
(14) Tian, X. B.; Chen, Y.; Chen, Y.; Chen, D.; Wang, Q.; Li, X. H. Removal of Gaseous Hydrogen Sulfide by a FeOCl/H_2O_2 Wet Oxidation System. *ACS Omega* **2022**, *7*, 8163−8173.
(15) Ullah, H.; Loh, A.; Trudgeon, D. P.; Li, X. Density Functional Theory Study of NiFeCo Trinary Oxy-Hydroxides for an Efficient and Stable Oxygen Evolution Reaction Catalyst. *ACS Omega* **2020**, *32*, 20517−20524.
(16) Lee, S. M.; Park, K. H.; Kim, S. S.; Kwon, D. W.; Hong, S. C. Effect of the Mn oxidation state and lattice oxygen in Mn-based TiO_2 catalysts on the low-temperature selective catalytic reduction of NO by NH_3. *J. Air Waste Manage. Assoc.* **2012**, *62*, 1085−1092.
(17) Pauly, N.; Yubero, F.; García-García, F. J.; Tougaard, S. Quantitative analysis of Ni 2p photoemission in NiO and Ni diluted in a SiO_2, matrix. *Surf. Sci.* **2016**, *644*, 46−52.
(18) Yang, J.; Ren, S.; Zhang, T.; Su, Z.; Long, H.; Kong, M.; Yao, L. Iron doped effects on active sites formation over activated carbon supported Mn-Ce oxide catalysts for low-temperature SCR of NO - Science Direct. *Chem. Eng. J.* **2020**, *379*, 122398.
(19) Wan, Q.; Duan, L.; He, K.; Li, J. Removal of gaseous elemental mercury over a CeO_2-WO_3/TiO_2 nanocomposite in simulated coal-fired flue gas. *Chem. Eng. J.* **2011**, *170*, 512−517.
(20) Wang, Y.; Liu, L.; Liu, Y. Oxidation Absorption of Hg^0 in the Gas Phase Using a Double Catalyzers-Double Oxidants Coactivation Technology. *Energy Fuels* **2022**, *36*, 2656.
(21) Li, J. F.; Yan, Q.; Qu, Z.; Qiao, S.; Yang, S.; Guo, Y.; Liu, P.; Jia, J. Catalytic Oxidation of Elemental Mercury over the Modified Catalyst Mn/α-Al_2O_3 at Lower Temperatures. *Environ. Sci. Technol.* **2010**, *44*, 426−431.
(22) Mullins, D. R.; Overbury, S. H.; Huntley, D. R. Electron spectroscopy of single crystal and polycrystalline cerium oxide surfaces. *Surf. Sci.* **1998**, *409*, 307−319.
(23) Liu, W.; Ai, Z.; Zhang, L. Design of a neutral three-dimensional electro-Fenton system with foam nickel as particle electrodes for wastewater treatment. *J. Hazard. Mater.* **2012**, *243*, 257−264.
(24) Fu, D. M.; Chen, J. P.; Liang, X. M. Wet air oxidation of nitrobenzene enhanced by phenol. *Chemosphere* **2005**, *59*, 905−908.
(25) Wang, J. B.; Fu, W. T.; He, X. W.; Yang, S.; Zhu, W. Catalytic wet air oxidation of phenol with functionalized carbon materials as catalysts: reaction mechanism and pathway. *J. Environ. Sci.* **2014**, *26*, 1741−1749.
(26) Oliviero, L.; Barbier, J.; Duprez, D. Wet Air Oxidation of nitrogen-containing organic compounds and ammonia in aqueous media. *Appl. Catal., B* **2003**, *40*, 163−184.
(27) Goff, G. S.; Rochelle, G. T. Monoethanolamine degradation: O_2 mass transfer effects under CO_2 capture conditions. *Ind. Eng. Chem. Res.* **2004**, *43*, 6400−6408.
(28) Wang, T.; Jens, K. J. Oxidative Degradation of Aqueous 2-Amino-2-methyl-1-propanol Solvent for Postcombustion CO_2 Capture. *Ind. Eng. Chem. Res.* **2012**, *51*, 6529−6536.
(29) Rooney, P. C.; Dupart, M. S.; Bacon, T. R. Oxygen's role in alkanolamine degradation. *Hydrocarbon Process.* **1998**, *77*, 109−113.
(30) Deng, H.; Lin, L.; Sun, Y.; Pang, C.; Zhuang, J.; Ouyang, P.; Li, J.; Liu, S. Activity and Stability of Perovskite-Type Oxide $LaCoO_3$ Catalyst in Lignin Catalytic Wet Oxidation to Aromatic Aldehydes Process. *Energy Fuels* **2009**, *23*, 19−24.

https://doi.org/10.1021/acsomega.2c08074
ACS Omega 2023, 8, 8683−8694